Improved methodology to compute the intrinsic friction coefficient at solid–liquid interfaces

View Online   Export Citation   CrossMark

Sleeba Varghese,[1,2] (iD) J. S. Hansen,[2] and B. D. Todd[1,a] (iD)

AFFILIATIONS

[1] Department of Mathematics, School of Science, Swinburne University of Technology, Melbourne, Victoria 3122, Australia
[2] "Glass and Time," IMFUFA, Department of Science and Environment, Roskilde University, Roskilde 4000, Denmark

Note: This paper is part of the JCP Special Topic on Fluids in Nanopores.
[a] Author to whom correspondence should be addressed: btodd@swin.edu.au

ABSTRACT

In this work, we propose an improved methodology to compute the intrinsic friction coefficient at the liquid–solid (L–S) interface based on the theoretical model developed by Hansen *et al.* [Phys. Rev. E **84**, 016313 (2011)]. Using equilibrium molecular dynamics, we apply our method to estimate the interfacial friction for a simple Lennard-Jones system of argon confined between graphene sheets and a system of water confined between graphene sheets. Our new method shows smaller statistical errors for the friction coefficient than the previous procedure suggested by Hansen *et al.* Since we only use the interfacial particles, the interfacial friction calculated using our method is solely due to the wall–fluid interactions and is devoid of bulk fluid contributions. The intrinsic nature of the friction coefficient has been validated by measuring the friction coefficient at different interfaces and channel sizes and against direct non-equilibrium molecular dynamics measurements. Our improved methodology is found to be more reliable than the existing equilibrium and non-equilibrium methods and does not suffer from the well-known convergence and correlation-time ambiguities in the methods formulated along Green–Kubo-like ideas.

Published under license by AIP Publishing. https://doi.org/10.1063/5.0040191

I. INTRODUCTION

The advent of nanofluidics has propelled research interest in the microscopic nature of confined fluid flows. Besides the academic interest, nanofluidics also offers enormous potential in the development of devices that can push the frontiers of technology, biology, and medicine.[1–4] Design and control of these nanofluidic devices requires a deep understanding of the fundamental behavior of the fluid flow through nanochannels. In the nanoscale regime, the classical (or standard) macroscale assumptions may become inadequate to predict the behavior of the fluid flow.[5–7] One important difference between the nanoscopic and the macroscopic hydrodynamics is due to non-zero contribution from the fluid slip at the liquid–solid (L–S) boundary, which under macroscale flows can be safely neglected. Hence, nanoscale flows require a more general slip boundary condition to accurately describe its flow behavior, unlike the "no-slip" boundary assumption typically employed in the macro-scale Navier–Stokes equation.

A theoretical basis for the slip phenomenon occurring at the L–S boundary was first given by Navier.[8] According to Navier, the degree of slip at a solid surface is proportional to the magnitude of tangential stress at the L–S interface. Assuming the fluid is confined in the z direction and flow is in the x direction, the Navier slip condition at a surface S whose unit normal points into the confined fluid is given as[9]

$$\sigma_{xz} = \xi_0 u_x(z) \text{ on } S \ (x, y, z \in S), \tag{1}$$

where σ_{xz} is the tangential stress tensor component exerted by the wall on the fluid, u_x is the x component of the velocity at a distance z away from the wall, and ξ_0 is the interfacial friction coefficient. Combining Eq. (1) with Newton's law of viscosity ($\sigma_{xz} = \eta_0 \frac{\partial u_x}{\partial z}$) and when $z \to z_{wall}$, we get

$$u_s = \left(\frac{\eta_0}{\xi_0}\right) \frac{\partial u_x}{\partial z}\bigg|_{z=z_{wall}} = L_s \frac{\partial u_x}{\partial z}\bigg|_{z=z_{wall}}, \tag{2}$$

where u_s is the slip velocity, η_0 is the shear viscosity, and $L_s = (\eta_0/\xi_0)$ is known as the slip length. Equation (2) represents the hydrodynamic boundary condition for a fluid flow with slip at the solid boundary.

From Eq. (2), it becomes clear that, to quantify the slip occurring at the boundary, we need to estimate the value of either ξ_0 or L_s. Note that while slip is omnipresent, it can safely be ignored at macroscopic length scales. The sub-nanometer size of the slip region makes an experimental estimation of these quantities difficult. This has led to the development of theoretical and computer simulation techniques to calculate the interfacial slip. Among the atomistic simulation techniques, molecular dynamics (MD) has evolved into a stable tool to investigate nanoscale flows. *In silico* experiments using MD follow two distinct methodologies, namely, non-equilibrium MD (NEMD) and equilibrium MD (EMD).

NEMD simulations involve the application of an external field to the system under consideration and analyzing the response of the system to this external field.[10] For example, NEMD methods for evaluating slip might involve generating a Hagen–Poiseuille flow or Couette flow by applying an external field to the confined fluid or wall.[11,12] On the other hand, EMD simulations use the equilibrium fluctuations of the system to gain insight into the behavior of the system in the zero external force limit.

Though NEMD simulations are widely used to calculate slip, the strength of the external field influences the slip length significantly. The slip length is reported to be constant for low shear rates but found to increase rapidly and diverge for higher shear rates.[13–15] If one is interested in simulations that match experiment, then typically one needs to perform many NEMD simulations at different field strengths and extrapolate to the linear regime, where the slip length is independent of the field strength. This makes NEMD evaluation of slip a computationally intensive process compared to its EMD counterpart. Besides the computational expense, a further complication also arises in the NEMD estimation of the slip length for high slip systems, such as water flowing in graphene nanochannels, in which the flat velocity profiles can lead to large errors in estimating the velocity tangent at the fluid–solid interface.[15] All these issues demand an EMD based methodology to obtain a reliable estimate for the slip at the interface.

Initial attempts to calculate the friction coefficient ξ_0 using EMD simulations were made by Bocquet and Barrat (BB).[16,17] In their 1994 paper,[16] Bocquet and Barrat derived a time correlation integral expression to calculate the equilibrium Navier friction coefficient given by

$$\xi_0 = \frac{1}{Ak_BT} \int_0^{t=\infty} C_{F_x^{tot}F_x^{tot}}(t)\,dt, \qquad (3)$$

where k_B is the Boltzmann constant, T is the temperature of the system, A is the surface area of the wall, F_x^{tot} is the x component of the total tangential force acting on the confined fluid due to the wall, and $C_{F_x^{tot}F_x^{tot}}(t) = \langle F_x^{tot}(t)F_x^{tot}(0) \rangle$ is the time correlation function at a correlation lag time, t. By deriving Eq. (3), BB did a commendable job in developing a theoretical methodology to calculate ξ_0 from the statistical fluctuations of the bulk fluid, similar to that of other transport coefficients. BB also verified the validity of their phenomenological model by comparing the values of time correlation functions in Eq. (3) with the data obtained from MD simulations.

Though the BB method has been widely used to calculate the friction coefficient of confined fluid flows, recent studies have reported that ξ_0 obtained using Eq. (3) only provides an effective value for the friction coefficient of the system instead of the intrinsic friction coefficient at the interface.[18–20] Another issue faced by this methodology is that the force autocorrelation in Eq. (3) provides a consistent plateau value of ξ_0 only if the thermodynamic limit is achieved for the system.[21,22] Though the BB method can provide appreciable results for semi-infinite cases where the fluid is in contact with a single solid boundary, a nanoconfined system usually consists of far fewer particles than the thermodynamic limit, which in turn means that the integral of the force autocorrelation for the finite system converges to zero as the correlation lag time t approaches infinity.[21,23,24] This is due to the fact that Green–Kubo formulations are only strictly valid in the zero wavevector limit, which is never the case for confined fluid systems. Hence, the friction coefficient calculated using Eq. (3) decays algebraically with increasing t. Though recent studies[25–29] have shown significant progress in finding solutions to the "the plateau problem" encountered in the BB method, an alternative theory that does not follow a Green–Kubo-like formalism and only considers the interfacial friction was considered a useful new development, such as that proposed by Sokhan and Quirke.[30]

Hansen *et al.*[19] investigated this issue and developed an alternative theoretical model to calculate the interfacial friction coefficient. In their model to maintain the interfacial integrity of the quantity, they considered the statistical fluctuations of a slab of particles (in a slab width of approximately one molecular diameter) close to the solid wall to estimate the value of the friction coefficient. For sufficiently small relative velocities between this slab and the wall, they proposed a Langevin type linear constitutive equation given by

$$F_x(t) = -\int_0^t \zeta(t-\tau)\Delta u_x(\tau)\,d\tau + F_r(t), \qquad (4)$$

where $F_x(t)$ is the wall–slab shear force at time t in the x direction, ζ is the friction kernel, and $\Delta u_x = u_{slab,x} - u_{wall,x}$ is the x component of relative velocity between the wall and the slab. For immobile walls, $\Delta u_x = u_{slab,x} = u_x$. F_r is a random force term that has zero mean and is uncorrelated with $u_{slab,x}$. The expression for steady flows is obtained by taking the time average of Eq. (4),

$$\langle F_x \rangle = -\zeta_0 \langle \Delta u_x \rangle = -\xi_0 A \langle \Delta u_x \rangle, \qquad (5)$$

where ξ_0 is the zero frequency friction coefficient or intrinsic friction coefficient and A is the surface area.

One important parameter that influences the value of the intrinsic friction coefficient is the width of the slab. If the slab width is not chosen appropriately, the friction coefficient calculated from the slab particles will include both frictional and viscous forces. Niavarani and Priezjev[31] reported that the density of the first fluid layer adjacent to the wall is a crucial component in determining the value of the friction coefficient. This observation was in accordance with previous MD studies, which also suggested a strong correlation between the slip length and the surface-induced order of the first fluid layer.[32–34] From these studies, we assume a slab width equal to the width of the first fluid density peak to predict the intrinsic friction coefficient of the confined system accurately.

Since ξ_0 in Eq. (5) is calculated from only the interfacial particles, the method proposed by Hansen et al.[19] may be considered as a local description to compute the interfacial friction coefficient, in that it does separate out the (local) interfacial frictional and more long-range viscous contributions of the fluid. However, implementation of this method can result in a poor statistical averaging due to the limited number of particles at the interface. In this work, we address this issue in the original work of Hansen et al.[19] and propose an alternate and statistically superior methodology to calculate the intrinsic friction coefficient at the boundary. Section II provides a detailed description of the derivation of our new method. After Sec. II, we discuss the computational details of this study, which is then followed by a section on the results and discussion.

II. THEORY

We start from the linear constitutive relation in Eq. (4), which when multiplied with $u_{slab,x}$ and ensemble averaged over different independent initial conditions gives us

$$C_{u_x F_x}(t) = -\int_0^t \zeta(t - \tau) C_{u_x u_x}(\tau) d\tau, \tag{6}$$

where $C_{u_x F_x}(t) = \langle u_x(0) F_x(t) \rangle$ and $C_{u_x u_x}(t) = \langle u_x(0) u_x(t) \rangle$ are the time correlation functions at a correlation lag time t. The Laplace transform of Eq. (6) converts the integral expression in the time domain into a more convenient algebraic expression in the s domain,

$$\tilde{C}_{u_x F_x}(s) = -\tilde{\zeta}(s) \tilde{C}_{u_x u_x}(s), \tag{7}$$

where s is the Laplace coordinate and the Laplace transform of a function $f(t)$ is defined as

$$L[f(t)] = \int_0^\infty f(t) e^{-st} dt = \tilde{f}(s). \tag{8}$$

From Eq. (7), we can compute the steady-state friction coefficient directly as

$$\xi_0 = \lim_{s \to 0} \frac{\tilde{\zeta}(0)}{A} = -\frac{1}{A} \frac{\tilde{C}_{u_x F_x}(0)}{\tilde{C}_{u_x u_x}(0)}. \tag{9}$$

However, the friction coefficient computed using Eq. (9), which we define as Method-1, has large statistical uncertainty due to the variability associated with the raw data. Hence, to reduce the statistical variability associated with $\zeta(s)$, Hansen et al.[19] approximated the friction kernel ζ to be a Maxwellian memory function[10] given by

$$\zeta(t) = \sum_{i=1}^n B_i e^{-\lambda_i t}. \tag{10}$$

They also reported that a one-term Maxwellian memory function was sufficient to describe the friction kernel for a simple fluid, i.e.,

$$\zeta(t) = B_1 e^{-\lambda_1 t}, \tag{11}$$

which implies

$$\tilde{\zeta}(s) = \frac{B_1}{s + \lambda_1}. \tag{12}$$

Note that for liquids with slower relaxation times, such as polymer melts or glassy systems, a single one-term Maxwellian function might not be sufficient. Substituting Eq. (12) in (7), we get

$$\tilde{C}_{u_x F_x}(s) = -\frac{B_1}{s + \lambda_1} \tilde{C}_{u_x u_x}(s). \tag{13}$$

A regression fit can be performed on Eq. (13) to compute the Maxwellian fitting parameters B_1 and λ_1, which are further used to compute the steady-state friction coefficient as

$$\xi_0 = \frac{\tilde{\zeta}(0)}{A} = \frac{B_1}{A \lambda_1}. \tag{14}$$

In this study, we propose an alternative methodology to compute the Maxwellian parameters, where instead of performing a regression fit to Eq. (13) we integrate along the Laplacian domain to compute B_1 and λ_1. From now on, we define the regression fit method as Method-2 and our new methodology, which we will describe in detail shortly and involves integrating $\tilde{\zeta}(s)$, as Method-3 for clarity. Figure 1 shows the schematic representation of the statistical dispersion associated with the Maxwellian parameters when computed using Method-2 and Method-3.

The variance associated with $\tilde{\zeta}(s) = \tilde{C}_{u_x F_x}(s) / \tilde{C}_{u_x u_x}(s)$ when calculated using Method-2 is given as

$$\sigma^2(s) = \frac{\sum_{k=1}^N \left(\tilde{\zeta}_k(s) - \bar{\tilde{\zeta}}(s) \right)^2}{N}, \tag{15}$$

where $\bar{\tilde{\zeta}}(s) = \frac{\sum_{k=1}^N \tilde{\zeta}_k(s)}{N}$ and N = number of independent simulations (i.e., trajectories). Thus, the mean of variance of $\sigma^2(s)$ for Method-2
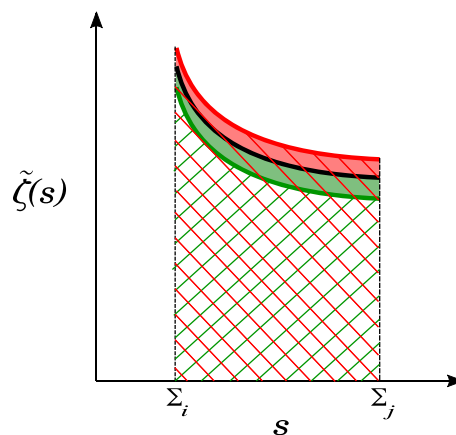

FIG. 1. Schematic representation of the variance involved with $\tilde{\zeta}(s)$ when computed using Method-2 and Method-3. The black solid curve represents the average $\tilde{\zeta}(s)$, computed over N independent trajectories. The red and green solid curves represent the upper and lower limits for $\tilde{\zeta}(s)$, respectively, and the shaded part corresponds to the region along which $\tilde{\zeta}(s)$ can vary. The red hashed region corresponds to the area under the red solid curve, and the green hashed region corresponds to the area under the green solid curve. Σ_i and Σ_j are arbitrary points in the domain of s.

when averaged over the entire s domain between arbitrary points Σ_i and Σ_j can be written as

$$S_{\text{M-2}}^{\text{Avg}} = \frac{\sum_{s=\Sigma_i}^{\Sigma_j} \sigma^2(s)}{n}, \tag{16}$$

where n = total number of data points in the s domain.

As we will shortly describe, our newly proposed Method-3 will involve integrating the $\tilde{\zeta}(s)$ curve. Hence, the statistical uncertainty is proportional to the variance of the area under the curve (AUC). The area under the curve (AUC_k) $\tilde{\zeta}_k(s)$ for each independent trajectory k is given as

$$\text{AUC}_k = \int_{\Sigma_i}^{\Sigma_j} \tilde{\zeta}_k(s)\,ds. \tag{17}$$

Hence, the mean of variance associated with Method-3 is given as

$$S_{\text{M-3}}^{\text{Avg}} = \frac{\sum_{k=1}^{N} \left(\text{AUC}_k - \text{AUC}_{\text{mean}}\right)^2}{N}, \tag{18}$$

where $\text{AUC}_{\text{mean}} = \frac{\sum_{k=1}^{N} \text{AUC}_k}{N}$ and again N is the number of independent trajectories.

Since the statistical fluctuations in the area under the curve will be smaller than the fluctuations in the curve itself, we conjecture here that

$$S_{\text{M-3}}^{\text{Avg}} < S_{\text{M-2}}^{\text{Avg}}, \tag{19}$$

which should result in better statistical precision for the computed interfacial friction coefficient. We will show this to be the case in Sec. IV.

To implement Method-3, Eq. (13) can be rearranged and integrated from an arbitrary minimum Σ_i to an arbitrary maximum Σ_j,

$$\int_{\Sigma_i}^{\Sigma_j} \frac{s + \lambda_1}{B_1} ds = -\int_{\Sigma_i}^{\Sigma_j} \frac{\tilde{C}_{u_x u_x}(s)}{\tilde{C}_{u_x F_x'}(s)} ds$$
$$\Rightarrow \frac{1}{B_1}\left[\frac{\Sigma_j^2 - \Sigma_i^2}{2} + \lambda_1(\Sigma_j - \Sigma_i)\right] = \Lambda, \tag{20}$$

where $\Lambda = -\int_{\Sigma_i}^{\Sigma_j} \frac{\tilde{C}_{u_x u_x}(s)}{\tilde{C}_{u_x F_x'}(s)} ds$, which can be numerically determined directly from EMD simulations.

To solve for the parameters B_1 and λ_1, we need two equations. This can be obtained by taking two different integral limits for Eq. (20), i.e., Σ_1 to Σ_2 and Σ_3 to Σ_4,

$$\frac{1}{B_1}\left[\frac{\Sigma_2^2 - \Sigma_1^2}{2} + \lambda_1(\Sigma_2 - \Sigma_1)\right] = \Lambda_1 \tag{21}$$

and

$$\frac{1}{B_1}\left[\frac{\Sigma_4^2 - \Sigma_3^2}{2} + \lambda_1(\Sigma_4 - \Sigma_3)\right] = \Lambda_2. \tag{22}$$

Dividing Eq. (21) by Eq. (22) and taking $\Lambda_1/\Lambda_2 = C$, we find

$$\left[\frac{\Sigma_2^2 - \Sigma_1^2}{2} + \lambda_1(\Sigma_2 - \Sigma_1)\right] = C\left[\frac{\Sigma_4^2 - \Sigma_3^2}{2} + \lambda_1(\Sigma_4 - \Sigma_3)\right]. \tag{23}$$

Rearranging Eq. (23), we get

$$\lambda_1 = \frac{\left(\Sigma_2^2 - \Sigma_1^2 - C(\Sigma_4^2 - \Sigma_3^2)\right)}{2\left(C(\Sigma_4 - \Sigma_3) - \Sigma_2 + \Sigma_1\right)}. \tag{24}$$

By substituting the value of λ_1 in Eq. (21) or (22), we can obtain the value of B_1. Finally, the fluid–solid intrinsic interfacial friction coefficient ξ_0 can be found by substituting the parameters B_1 and λ_1 in Eq. (14).

III. METHODOLOGY

We perform molecular dynamics simulations using the large atomic/molecular massively parallel simulator[35] (LAMMPS) package to verify the reliability of our new methodology. The friction coefficient at the liquid–solid interface was investigated for two different model systems, namely, argon and water confined in graphene nanochannels. Schematic illustration of the confined system is shown in Fig. 2, where graphene sheets are placed in the x–y plane with periodicity in both directions and confinement along the z axis.

Each wall consists of three layers of stacked uncharged graphene sheets kept at an interlayer distance of 3.4 Å. The outermost layer at each wall is kept fixed to maintain a constant system size. The dimensions for the graphene nanochannel in the x–y plane are L_x = 36.87 Å and L_y = 35.61 Å. The intralayer carbon interactions for the graphene sheets were modeled using the optimized Tersoff potential.[36,37] A weak Lennard-Jones (L-J) potential is also applied between the interlayer carbon atoms to hold the graphene sheets together.[14,15]

The fluid–fluid (argon–argon) and fluid–wall (argon–carbon) interactions in the argon–graphene system are modeled using a truncated and shifted Lennard-Jones (L-J) potential,

$$\phi_{tr} = \begin{cases} 4\epsilon\left[\left(\dfrac{\sigma}{r_{ij}}\right)^{12} - \left(\dfrac{\sigma}{r_{ij}}\right)^6\right] - \phi(r_c) & \text{if } r_{ij} \leq r_c \\ 0 & \text{if } r_{ij} > r_c, \end{cases} \tag{25}$$

where r_{ij} is the interatomic distance between atoms i and j, and σ and ε are the length scale and interaction strength, respectively. The interaction cutoff r_c is kept at 10 Å. The values of the L-J parameters for the argon–graphene system are given in Table I. The fluid–wall L-J parameters are derived using the Lorentz–Berthelot rule. Argon is filled inside the graphene nanochannel at an average density of 1361.8 kg m^{-3}. The simulated state point for argon in our argon–graphene system corresponds to the state point with reduced density $\rho^* = 0.8$ and a reduced temperature $T^* = 1.0$ in the study by Rowley and Painter.[38]

For the water–graphene system, we use the SPC/E[39,40] water model with the bond and angles of each water molecule constrained using the SHAKE[41] algorithm in LAMMPS.[35] Each hydrogen atom in the water molecule carries a partial charge of 0.4238e, and an oxygen atom carries a partial charge of $-0.8476e$, where e is the elementary charge of an electron. The water–carbon interaction parameters are taken from the study of Werder et al.[42] The L-J parameters for the water–graphene system are given in Table II.
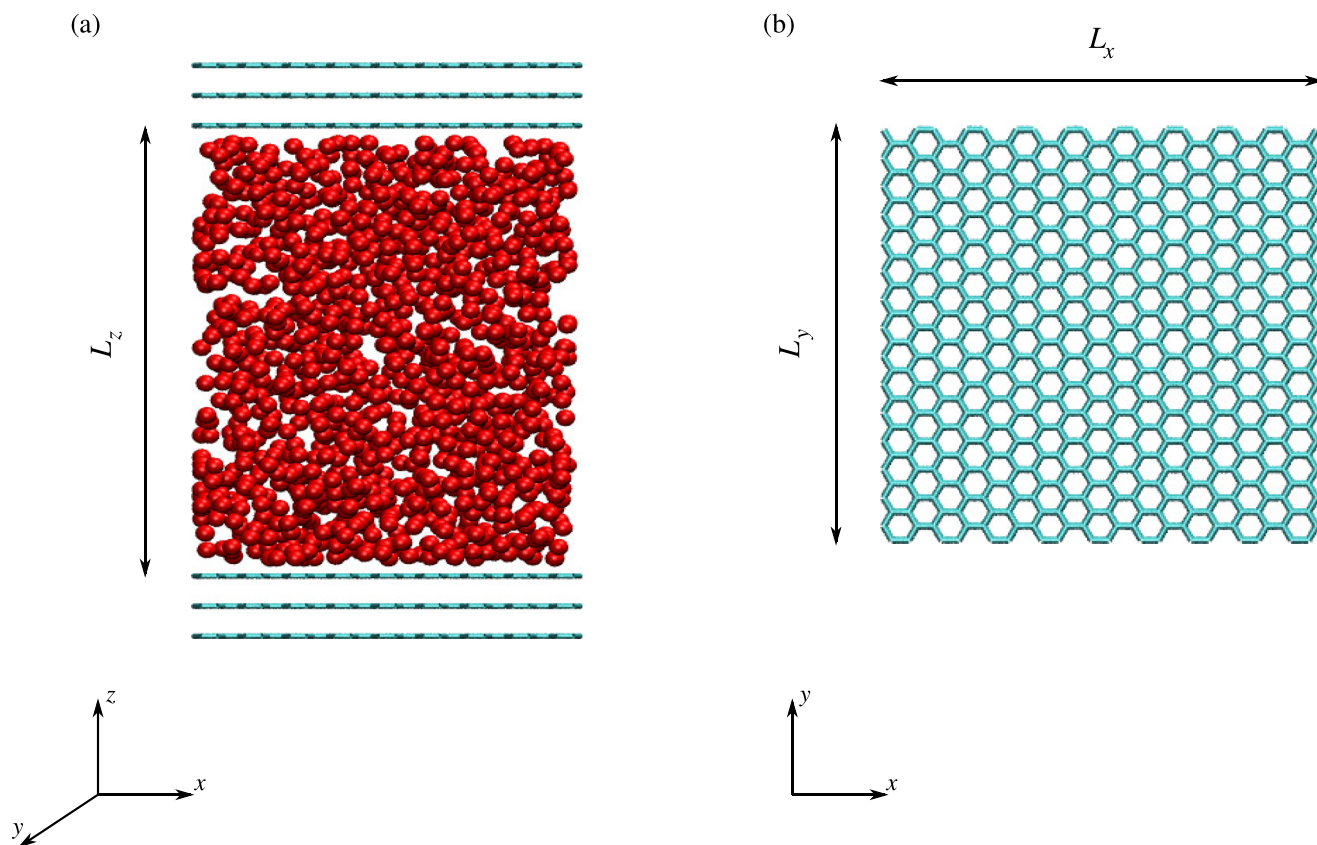
FIG. 2. (a) Schematic representation of the confined system. (b) Top view of the graphene channel.

The interaction cutoffs for Lennard-Jones and short-range Coulombic interactions were both kept at 10 Å. The long-range electrostatic interactions are calculated using the Ewald algorithm with the particle–particle–particle–mesh solver[43] of LAMMPS[35,44] with a relative root mean square error in the per-atom force calculations below 1×10^{-6}. To accommodate the non-periodicity in the z direction, we use the corrected Ewald algorithm EW3DC,[44] where the ratio of extended volume to actual channel size is set as 3.0.

The equations of motion for all particles are integrated using the Velocity-Verlet[45] scheme of LAMMPS[35] with an integration time step $\Delta t = 1$ fs. The total simulation run time for the argon–graphene system is 6 ns. The initial 2.0 ns is used to equilibrate the argon–graphene system at 120 K in the canonical

(NVT) ensemble by thermostating the walls using a Langevin thermostat.[46] After equilibration, a further 2.0 ns run in the microcanonical (NVE) ensemble is performed to verify the stability of the argon–graphene system. The final 2.0 ns is used to collect data for post-processing. For the water–graphene system prior to the equilibration at a constant temperature, the channel width is adjusted to maintain an internal pressure of 1 bar by fixing the bottom wall and using the top wall as a piston to apply pressure at 300 K. After setting the internal pressure, the water–graphene system is equilibrated for 2.0 ns at 300 K by thermostating the walls using the Langevin thermostat.[46] The equilibration stage is followed by a 2.0 ns run in the (NVE) ensemble to verify the system stability, and a final 2.0 ns run is performed to collect the data for post-processing. 50 independent

TABLE I. Interaction parameters for the argon–graphene system. The distance between inner-most graphene sheets for the system is $L_z = 51$ Å.

$\sigma_{Ar\text{-}Ar}$ (Å)	$\sigma_{Ar\text{-}C}$ (Å)	$\sigma_{C\text{-}C}$ (Å)	$\varepsilon_{Ar\text{-}Ar}$ (kcal/mol)	$\varepsilon_{Ar\text{-}C}$ (kcal/mol)	$\varepsilon_{C\text{-}C}$ (kcal/mol)
3.4	3.4	3.4	0.238 46	0.115 18	0.055 641

TABLE II. Interaction parameters for the water–graphene system. The C–C interaction parameters are the same as in Table I, and the distance between the inner-most graphene sheets is $L_z = 40.898$ Å.

$\sigma_{O\text{-}O}$ (Å)	$\sigma_{H\text{-}(O,H,C)}$ (Å)	$\sigma_{O\text{-}C}$ (Å)	$\varepsilon_{O\text{-}O}$ (kcal/mol)	$\varepsilon_{H\text{-}(O,H,C)}$ (kcal/mol)	$\varepsilon_{O\text{-}C}$ (kcal/mol)
3.166	0.0	3.19	0.155 35	0.0	0.093 69

simulations for argon–graphene and water–graphene systems were performed to obtain sufficient statistics.

IV. RESULTS AND DISCUSSION

The validity of the constitutive equation in Eq. (4) depends on the width of the slab chosen. Niavarani and Priezjev[31] showed that the fluid layer adjacent to the wall has a crucial role in determining the value of the friction coefficient. From Fig. 3, we observe that the first fluctuation in the fluid density for both systems extends approximately up to 5 Å away from the wall. Hence, we consider a slab of particles 5 Å away from each wall to calculate ξ_0. We further note that the choice of slab width was discussed in detail by Hansen et al.[19] and we refer the reader to this for further information.

Now, we calculate the friction coefficient at the L–S interface using the different methods derived from the model proposed by Hansen et al.[19] The initial step of each method transforms the time correlation functions defined in Eq. (6) into the Laplacian space. We only consider the Laplace domain ranging from $s = 0$ to 1.0 for our present study where the single term Maxwellian function for the friction kernel can be justified, as previously demonstrated.[19] Figure 4 shows an example of a time correlation function defined in Eq. (6) and their corresponding Laplace transform. For the first method, defined as Method-1, we calculate ξ_0 directly from Eq. (9) without considering any functional form for the friction kernel, whereas for the second method (Method-2), we compute the friction coefficient from the Maxwellian parameters using Eq. (14). The Maxwellian fitting parameters are computed from the regression fit of Eq. (13),

where $\tilde{C}_{u_x F_x}(s)$ and $\tilde{C}_{u_x u_x}(s)$ are obtained by transforming the simulation data into the Laplace space, which ranges from $s = 0$ to 1.0. Finally, our new method (Method-3) calculates the parameters in Eq. (14) from the algebraic expressions given via Eqs. (20)–(24). For Method-3, the integral limits for the Laplacian domain in Eqs. (21) and (22) were taken as $\Sigma_1 = 0$, $\Sigma_2 = \Sigma_3 = 0.5$, and $\Sigma_4 = 1$.

A parameter that significantly affects the reliability of the value of friction coefficient obtained using equilibrium methods is the choice at which the upper limit of correlation lag time t in Eqs. (3) and (6) should be truncated. In the case of the BB method, as t in Eq. (3) increases, the value of the friction coefficient decreases and is thus ambiguous. Now to investigate the influence of this issue on our methodology, we compare the friction coefficient values from the correlation functions truncated at different correlation lag times. Figures 5(a) and 5(b) plot the friction coefficient values computed at different correlation lag times for argon–graphene and water–graphene systems, respectively. Since the confined system consists of two walls and we perform 50 independent simulations, there will be 100 values of friction coefficient to average from, for each correlation lag time plotted in Fig 5. Though all three methods show similar results for shorter times, ξ_0 calculated using Method-1 and Method-2 becomes statistically less reliable as the correlation lag time increases, whereas Method-3 shows consistent values of friction coefficient over the entire range of correlation lag times with smaller statistical errors than Method-1 and Method-2. To quantify the statistical consistency of our new methodology, we also plot a histogram distribution of the friction coefficient values over all the correlation lag times in Figs. 5(c) and 5(d) and observe that the least statistical dispersion is shown by Method-3. The reason
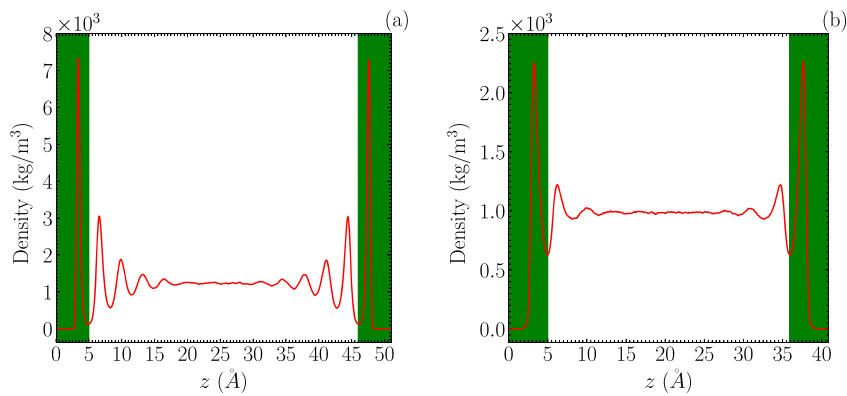
FIG. 3. (a) Density profile for the argon–graphene system. (b) Density profile for the water–graphene system. The green shaded region represents the slab width.
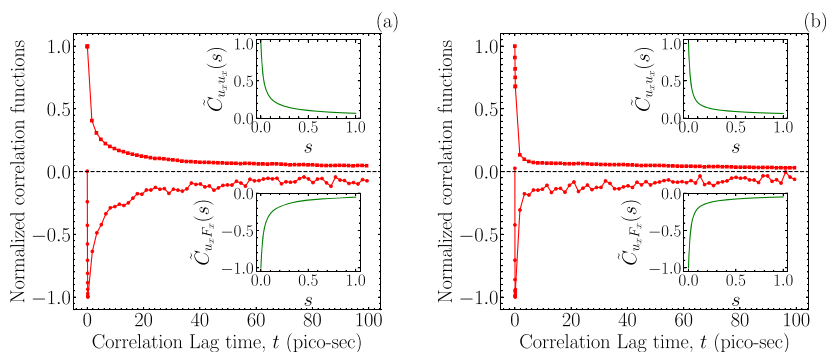
FIG. 4. Normalized time correlation functions for (a) argon–graphene and (b) water–graphene systems. Red filled squares represent $C_{u_x u_x}(t)$, and red filled circles represent $C_{u_x F_x}(t)$. The inset plot represents the corresponding normalized Laplace transform.
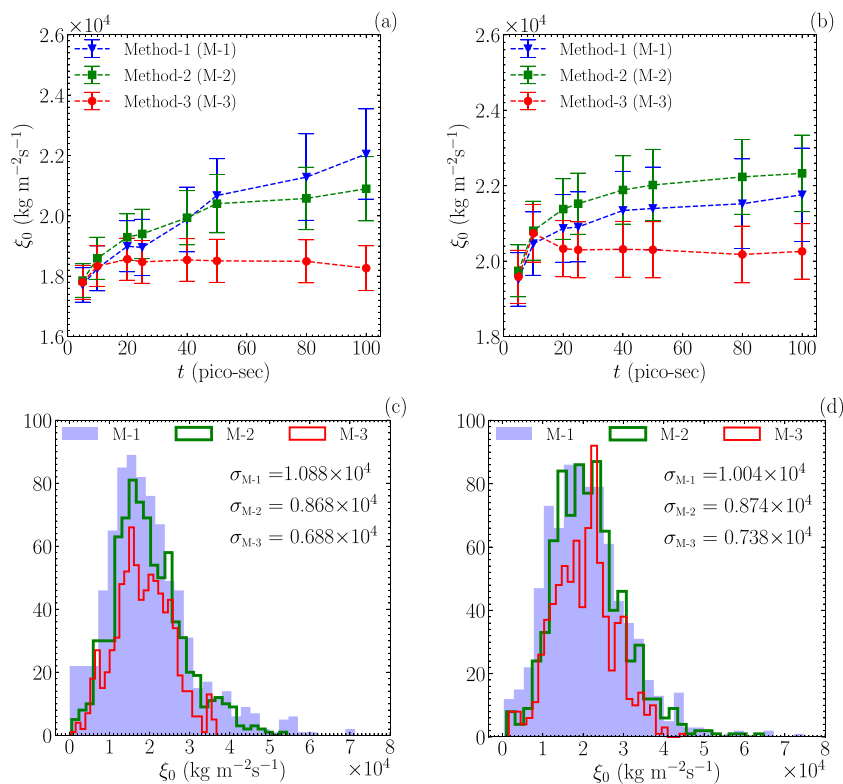
FIG. 5. First row: variation of friction coefficient with correlation time intervals for (a) argon–graphene and (b) water–graphene systems. The correlation lag times studied are t = 5, 10, 20, 25, 40, 50, 80, and 100 ps. The error bar for each correlation lag time is obtained from a set of 100 values of friction coefficient and denotes one standard error. Second row: histogram distribution of friction coefficient values for (c) argon–graphene and (d) water–graphene systems. The total number of data points under each histogram is 800. σ represents the standard deviation of the distribution.

behind this statistical superiority of Method-3 can be explained from Fig. 6, which shows S_{M-2}^{Avg} and S_{M-3}^{Avg} at different correlation lag times. As we conjectured earlier, $S_{M-3}^{Avg} < S_{M-2}^{Avg}$ for all correlation lag times, which in turn supports our starting hypothesis and demonstrates the improvement of our new methodology.

We now apply our method to calculate the friction coefficient with different solid–fluid interactions for the argon–graphene system. The wall–fluid potential is varied using a relative parameter $\varepsilon_r = \varepsilon_{sf}/\varepsilon_{ff}$, where ε_{sf} and ε_{ff} are the interaction strengths between solid–fluid and fluid–fluid particles in the system, respectively. We investigate three different wall–fluid interaction strengths (ε_{sf}) with

ε_r = 0.3, 0.5, and 1.0. The fluid–fluid interaction strength (ε_{ff}) is always taken as 0.238 46 kcal/mol. Figure 7(a) shows the variation of the intrinsic friction coefficient for the different wall–fluid interactions, and from the figure, it is evident that the more energetically favorable the solid–fluid interaction is, the larger the friction coefficient becomes. This inference confirms the reliability of our methodology in the investigation of the interfacial friction for different surface–liquid interactions.

We also verify the channel size independence of our methodology by calculating the friction coefficient for two different argon–graphene system sizes, L_z = 51 Å (15σ) and 102 Å (30σ).
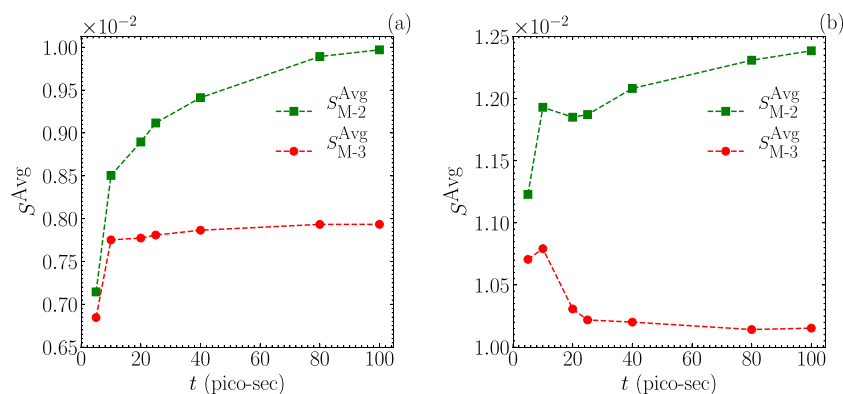

FIG. 6. Average variance in Methods 2 and 3, as defined by Eqs. (16) and (18), at different correlation lag times for the (a) argon–graphene system and (b) water–graphene system.
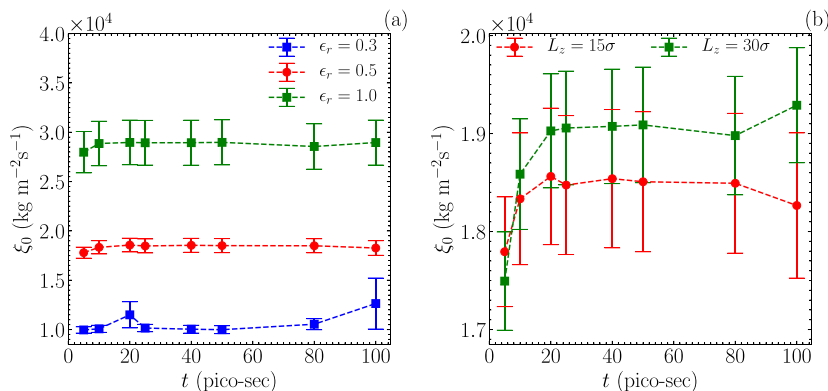
FIG. 7. (a) Variation of friction coefficient with varying wall–fluid interaction strength. (b) Variation of friction coefficient for different channel widths and $\sigma = \sigma_{Ar\text{-}Ar} = 3.4$ Å.

From Fig. 7(b), we can conclude that the friction coefficient calculated using our method is system size independent. Hence, Figs. 7(a) and 7(b) combined satisfy the conditions suggested by Cieplak *et al.*[47] for an equilibrium slip quantity to be an intrinsic property of the solid–fluid interface.

The frequency-dependence of the friction coefficient can be obtained by taking the Fourier transform of the friction kernel defined in Eq. (10),

$$\zeta(\omega) = \frac{B_1 \lambda_1}{\lambda_1^2 + \omega^2} - i \frac{B_1 \omega}{\lambda_1^2 + \omega^2}, \qquad (26)$$

where ω is the angular frequency. Figure 8 shows the variation of the real and imaginary components of the friction kernel with ω for the argon–graphene system with three different L–S interfaces. As expected, the real component for all systems decreases monotonically. However, for the imaginary component, we observe that the higher the value of the steady state interfacial friction ($\xi_0^{0.3} < \xi_0^{0.5} < \xi_0^{1.0}$) of the system, the larger is the shift in the peak frequency (ω_p) to the right, i.e., $\omega_p^{0.3} < \omega_p^{0.5} < \omega_p^{1.0}$. This is indicative of the effect the L–S interface has on the shear relaxation of the confined fluid, which can have significant interest in the study of oscillatory flows.
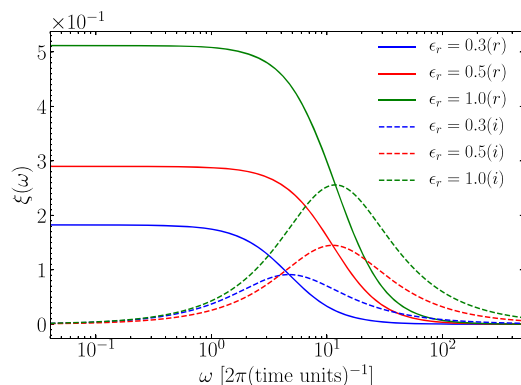
Now, we compare Method-3 with the existing methods for slip estimation. For the EMD comparison of the slip, we use the BB method defined in Eq. (3) to compute the friction coefficient. For Eq. (3), BB commented that the choice of the upper limit of the correlation lag time t should be made judiciously to avoid spurious results for ξ_0. This is because the integral of the force autocorrelation function for a finite system vanishes to zero in the infinite time limit.[21,23,24] A viable workaround to this issue is to consider ξ_0 only up to the correlation lag time that shows a plateau for the integrated force autocorrelation function.[48,49] From Fig. 9, we observe that the plateau behavior for the running integral of ξ_0 is shown only up to $t = 5$ ps, beyond which there is no observable plateau. Hence, for the BB method, we will use the value of friction coefficient at $t = 5$ ps for comparison. In addition, from the inset plots in Fig. 9, we can see that Method-3 provides more consistent values of friction coefficient at different correlation lag times compared to the BB method.

To verify our EMD calculations, we perform NEMD simulations on both argon–graphene and water–graphene systems. For the NEMD calculations, we simulate a Hagen–Poiseuille flow by applying an external field to the confined fluid. We perform 20 independent simulations at each external field to obtain sufficient averaging for the results. We used the same thermodynamic conditions for NEMD simulations similar to our EMD simulations, i.e., 120 K for the argon–graphene system and 300 K for the water–graphene system. The systems were maintained at the required temperature by thermostating the walls using the Langevin thermostat.[46]

Even though the slip at the L–S boundary is quantified by the slip length, systems with high slip generate a flat velocity profile, which can in turn lead to large errors in the NEMD slip length estimation, as described by Kannam *et al.*[15] An alternative method based on classical hydrodynamics is to compute the NEMD friction coefficient and from that use the definition of the slip length as the ratio of the shear viscosity to the friction coefficient to estimate the slip length. Hence, to estimate the NEMD friction coefficient, we use the Navier slip relation in Eq. (1),

$$\sigma_{xz} = \tau = \xi_0 u_s. \qquad (27)$$

The frictional shear stress at the wall–liquid interface τ is given as[50]

$$\tau = \frac{N m F_e}{2A}, \qquad (28)$$

FIG. 8. Complex frequency dependent friction coefficient $\xi(\omega)$ for different systems. The solid and dashed lines indicate the variation of real (r) and imaginary (i) parts of the friction coefficient, respectively.
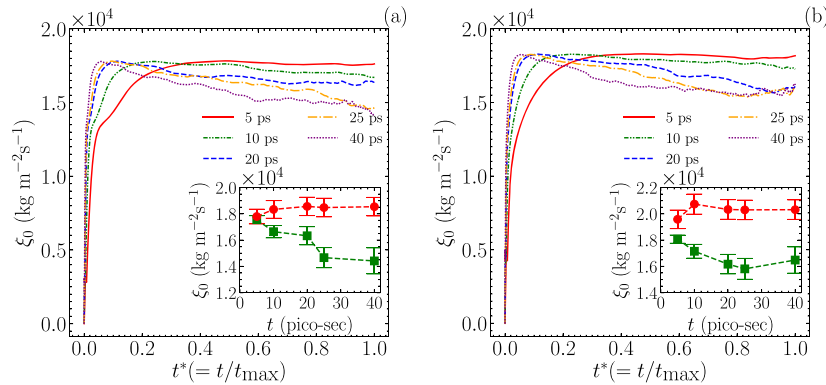
FIG. 9. (Main plot) Friction coefficient calculated for different correlation time intervals, calculated using the BB method for (a) argon–graphene and (b) water–graphene systems. The correlation times in the horizontal axis are normalized with respect to their maximum value for better representation. The running integral for each correlation lag time is averaged from a dataset of size 100 (50 independent simulations for two walls). (Inset plot) Variation of friction coefficient with correlation lag times for (red filled circle) Method-3 and (green filled square) BB method. The error bars denote one standard error.
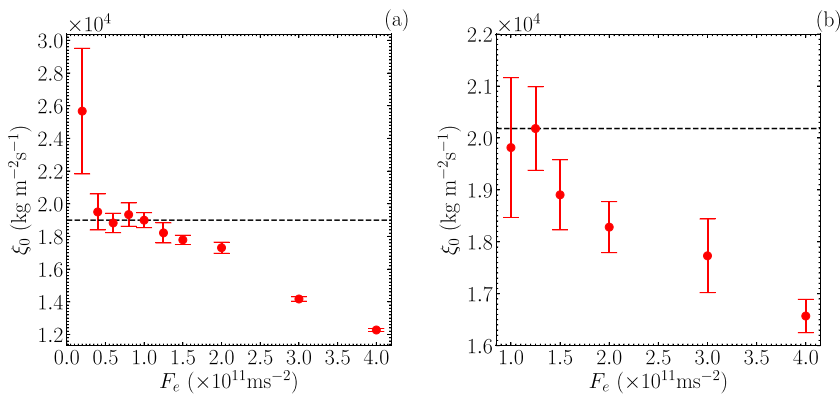

FIG. 10. NEMD estimated friction coefficient as a function of the external field (force per unit mass, i.e., acceleration) for (a) argon–graphene and (b) water–graphene systems. The hashed horizontal line represents the average value of ξ_0 at the critical external field, which is $\sim 1 \times 10^{11}$ ms^{-2} for argon–graphene and $\sim 1.25 \times 10^{11}$ ms^{-2} for water–graphene systems.
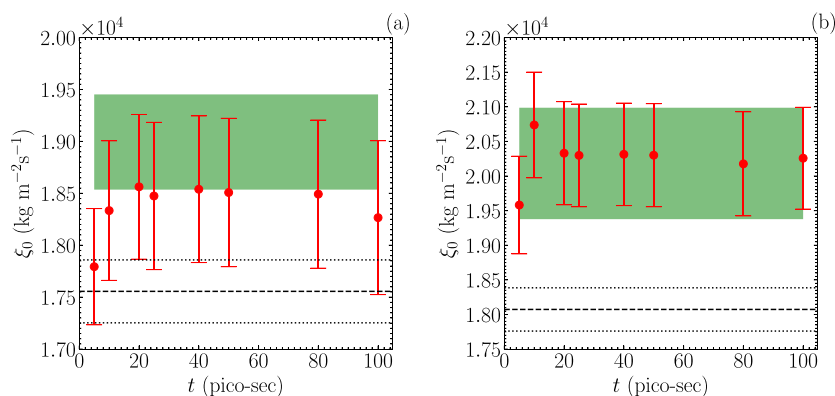

FIG. 11. Comparison of ξ_0 calculated using different methods for (a) argon–graphene and (b) water–graphene systems. Red filled circles represent ξ_0 calculated using Method-3 at different correlation lag intervals. The dashed line shows the average ξ_0 calculated using the BB method at the correlation lag time $t = 5$ ps, and the dotted lines correspond to the upper and lower limits of the BB friction coefficient. The green shaded region represents the NEMD friction coefficient range at the critical external field, i.e., $\sim 1 \times 10^{11}$ ms^{-2} for argon–graphene and $\sim 1.25 \times 10^{11}$ ms^{-2} for water–graphene systems.

where N is the number of molecules, m is the molecular mass, F_e is the external applied field, and A is the wall surface area. The slip velocity u_s is obtained by fitting the velocity profile from the NEMD simulations with a quadratic expression

$$u_x(z) = az^2 + b, \tag{29}$$

where a and b are the fitting parameters. Hence, the slip velocity is calculated from the end points of the fitted parabola in Eq. (29) as

$$u_s = \frac{u_x(-L_z/2) + u_x(L_z/2)}{2}, \tag{30}$$

where L_z is the channel width. Note here, however, that this estimation of the slip velocity, and hence the friction coefficient, is based on an assumption that the velocity profile is strictly parabolic, which is not true for highly confined fluids.[51] It is for reasons such as this, as well as non-local viscosity effects for highly confined fluids,[11] that make *a priori* statistical mechanics calculations of the friction coefficient and estimates of slip length preferable.

Figure 10 plots the NEMD estimates of friction coefficient as a function of the applied external field (the force per unit mass, i.e., the acceleration). It is clear from the figure that the friction coefficient diverges beyond a critical value of the external field, which is the limit wherein we can safely assume we are within the linear regime. Hence, we compare the NEMD friction coefficient within the critical external field limit with our EMD calculations, as shown in Fig. 11. From Figs. 11(a) and 11(b), we find that ξ_0 calculated using Method-3 provides closer agreement to the NEMD friction coefficient compared to the BB method.

V. CONCLUSION

Quantifying the friction at the solid–liquid interface is essential in the efficient design of micro/nanofluidic devices. In this work, we derived an EMD methodology (Method-3) to calculate the intrinsic friction coefficient at the liquid–solid boundary, based on the theoretical model proposed by Hansen *et al.*[19] The present methodology calculates the friction coefficient by integrating with respect to the Laplace coordinate of the time correlation functions, resulting in a statistically more precise value of friction coefficient based on the model of Hansen *et al.*[19] Since we use only the first adjacent fluid layer to the wall, the friction coefficient calculated using our method is an intrinsic property of the solid–fluid interface. The friction coefficient calculated using our method is sensitive to the wall–fluid interactions, and independent of the channel size, verifying the intrinsic nature of the proposed methodology.[47] We also observe that Method-3 provides the best fit to the NEMD friction coefficient in the linear regime. Since Method-3 provides consistent estimates for the friction coefficient solely based on the interfacial particles, we present our improved methodology as an effective alternative to the traditional NEMD and EMD methods to compute the slip or friction at the L–S interface. We furthermore observed that the magnitude of the steady-state friction coefficient has a significant influence on the shear relaxation of a confined fluid. Future investigations will look more into understanding the influence of surface properties on the frequency-dependent friction coefficient of confined flows.

Also in the future, we intend to apply our method to calculate the interfacial friction for more complex systems, such as confined lubricants or ionic systems. Since the proposed methodology does not require the convergence of time correlation functions, we expect to obtain statistically consistent values for the intrinsic friction coefficient even for slowly relaxing systems, such as long-chain polymeric fluids, with suitable modifications to the theory.

DATA AVAILABILITY

The data that support the findings of this study are available from the corresponding author upon reasonable request.

REFERENCES

[1]R. B. Schoch, J. Han, and P. Renaud, Rev. Mod. Phys. **80**, 839 (2008).
[2]J. C. T. Eijkel and A. van den Berg, Microfluid. Nanofluid. **1**, 249 (2005).
[3]L. Bocquet and E. Charlaix, Chem. Soc. Rev. **39**, 1073 (2010).
[4]W. Sparreboom, A. van den Berg, and J. C. T. Eijkel, New J. Phys. **12**, 015004 (2010).
[5]J. S. Hansen, J. C. Dyre, P. J. Daivis, B. D. Todd, and H. Bruus, Phys. Rev. E **84**, 036311 (2011).
[6]J. S. Hansen, J. C. Dyre, P. Daivis, B. D. Todd, and H. Bruus, Langmuir **31**, 13275 (2015).
[7]G. Karniadakis, A. Beskok, and N. Aluru, *Microflows and Nanoflows: Fundamentals and Simulation* (Springer Science & Business Media, 2006), Vol. 29.
[8]C. Navier, Mem. Acad. Sci. Inst. Fr. **6**, 1827 (1827).
[9]L. G. Leal, *Advanced Transport Phenomena: Fluid Mechanics and Convective Transport Processes* (Cambridge University Press, 2007), Vol. 7.
[10]D. J. Evans and G. P. Morriss, *Statistical Mechanics of Nonequilibrium Liquids* (ANU Press, 2007).
[11]B. D. Todd and P. J. Daivis, *Nonequilibrium Molecular Dynamics: Theory, Algorithms and Applications* (Cambridge University Press, 2017).
[12]M. Heiranian and N. R. Aluru, ACS Nano **14**, 272 (2019).
[13]P. A. Thompson and S. M. Troian, Nature **389**, 360 (1997).
[14]S. K. Kannam, B. D. Todd, J. S. Hansen, and P. J. Daivis, J. Chem. Phys. **135**, 144701 (2011).
[15]S. K. Kannam, B. D. Todd, J. S. Hansen, and P. J. Daivis, J. Chem. Phys. **136**, 024705 (2012).
[16]L. Bocquet and J.-L. Barrat, Phys. Rev. E **49**, 3079 (1994).
[17]L. Bocquet and J.-L. Barrat, J. Chem. Phys. **139**, 044704 (2013).
[18]J. Petravic and P. Harrowell, J. Chem. Phys. **127**, 174706 (2007).
[19]J. S. Hansen, B. D. Todd, and P. J. Daivis, Phys. Rev. E **84**, 016313 (2011).
[20]K. Huang and I. Szlufarska, Phys. Rev. E **89**, 032119 (2014).
[21]P. Español and I. Zúñiga, J. Chem. Phys. **98**, 574 (1993).
[22]L. Bocquet, J.-P. Hansen, and J. Piasecki, J. Stat. Phys. **89**, 321 (1997).
[23]R. Fisher and R. Watts, Aust. J. Phys. **25**, 21 (1972).
[24]S. I. Smedley and L. V. Woodcock, J. Chem. Soc., Faraday Trans. 2 **70**, 955 (1974).
[25]P. Español, J. A. de la Torre, and D. Duque-Zumajo, Phys. Rev. E **99**, 022126 (2019).
[26]H. Nakano and S.-i. Sasa, J. Stat. Phys. **176**, 312 (2019).
[27]H. Oga, Y. Yamaguchi, T. Omori, S. Merabia, and L. Joly, J. Chem. Phys. **151**, 054502 (2019).

[28] J. A. de la Torre, D. Duque-Zumajo, D. Camargo, and P. Español, Phys. Rev. Lett. **123**, 264501 (2019).

[29] H. Nakano and S.-i. Sasa, Phys. Rev. E **101**, 033109 (2020).

[30] V. P. Sokhan and N. Quirke, Phys. Rev. E **78**, 015301 (2008).

[31] A. Niavarani and N. V. Priezjev, Phys. Rev. E **77**, 041606 (2008).

[32] J.-L. Barrat and L. Bocquet, Faraday Discuss. **112**, 119 (1999).

[33] P. A. Thompson and M. O. Robbins, Phys. Rev. A **41**, 6830 (1990).

[34] N. V. Priezjev, Phys. Rev. E **75**, 051605 (2007).

[35] S. Plimpton, J. Comput. Phys. **117**, 1 (1995).

[36] J. Tersoff, Phys. Rev. B **39**, 5566 (1989).

[37] L. Lindsay and D. A. Broido, Phys. Rev. B **81**, 205441 (2010).

[38] R. L. Rowley and M. M. Painter, Int. J. Thermophys. **18**, 1109 (1997).

[39] H. J. C. Berendsen, J. R. Grigera, and T. P. Straatsma, J. Phys. Chem. **91**, 6269 (1987).

[40] Y. Wu, H. L. Tepper, and G. A. Voth, J. Chem. Phys. **124**, 024503 (2006).

[41] J.-P. Ryckaert, G. Ciccotti, and H. J. C. Berendsen, J. Comput. Phys. **23**, 327 (1977).

[42] T. Werder, J. H. Walther, R. L. Jaffe, T. Halicioglu, and P. Koumoutsakos, J. Phys. Chem. B **107**, 1345 (2003).

[43] R. W. Hockney and J. W. Eastwood, *Computer Simulation Using Particles* (McGraw-Hill, New York, 1981).

[44] I.-C. Yeh and M. L. Berkowitz, J. Chem. Phys. **111**, 3155 (1999).

[45] W. C. Swope, H. C. Andersen, P. H. Berens, and K. R. Wilson, J. Chem. Phys. **76**, 637 (1982).

[46] C. L. Brooks, J. Solution Chem. **18**, 99 (1989).

[47] M. Cieplak, J. Koplik, and J. R. Banavar, Phys. Rev. Lett. **86**, 803 (2001).

[48] K. Falk, F. Sedlmeier, L. Joly, R. R. Netz, and L. Bocquet, Nano Lett. **10**, 4067 (2010).

[49] G. Tocci, L. Joly, and A. Michaelides, Nano Lett. **14**, 6872 (2014).

[50] B. D. Todd, D. J. Evans, and P. J. Daivis, Phys. Rev. E **52**, 1627 (1995).

[51] K. P. Travis, B. D. Todd, and D. J. Evans, Phys. Rev. E **55**, 4288 (1997).